Numerical and Experimental Study of a Biomimetic UAV with Grids

R. Bardera
A.A. Rodriguez-Sevillano*
E. Barroso
J.C. Matias
J. Muñoz

SPAIN
Instituto Nacional de Técnica Aeroespacial (INTA), Torrejon de Ardoz, Madrid, 28850.
*Escuela Técnica Superior de Ingeniería Aeronáutica y del Espacio (ETSIAE-UPM), Madrid, 28040.

barderar@inta.es

ABSTRACT

Primary feathers of birds are commonly considered an elongation of the wings to improve the aerodynamic performance of birds by reducing the induced drag. In this paper a numerical and experimental analysis of an Unmanned Aerial Vehicle (UAV) inspired on the primary feathers of an eagle is presented. This biomimetic UAV presents a rectangular wing with three winglets at the tip of the wing to modify the lift distribution over the wing. Two UAV configurations have been studied: retracted and extended grids. Aerodynamic forces are measured in a low-speed wind tunnel by using a six-component force transducer. The Ansys-Fluent software is used to solve the Navier-Stoke equations. An increase in aerodynamic efficiency is achieved with the extended grids configuration for cruise and loiter phases.

1.0 INTRODUCTION

Historically, researchers and engineers have been inspired on the excellent flight performance of many flying biological organisms (e.g. birds, bats, insects) [1]. Slotted feathers on the wing tip are discovered in certain birds (vultures, eagles, hawks, condors and ospreys) and are considered an elongation of the wing to increase flight efficiency [2-3]. Previous investigations have analyzed slotted feathered wing tip to reduce induced drag and increase the aerodynamic efficiency. One example is the work of Tucker [4] who obtained a reduction in the induced drag on a wing with four primary feathers from a Harris' hawk in a wind tunnel. Another example is the study performed by KleinHeerenbrik and et.al [5] where they measured the airflow around a slotted wing tip of a jackdaw by using particle image velocimetry in a wind tunnel and obtained an increase in aerodynamic efficiency.

Aircraft vehicles that simulate the flying of these animals have become one of the most attractive aviation technologies [6-7]. In particular, the development of bio-inspired Unmanned Aerial Vehicles (UAVs) plays an important role in the international aerospace field, as they have the excellent advantage of flying without a pilot in multiple military and civilian operations (resulting in a reduced human risks) and are characterized by high aerodynamic performances and low manufacturing costs [8-9]. In recent decades, bio-inspired UAVs have been developed with different configurations and capabilities (in terms of autonomy, range and flight altitude) depending on the mission [10-14]. This study is focused on a 500 mm UAV inspired on the primary feathers of birds designed between the Instituto Nacional de Técnica Aeroespacial (INTA) and the Escuela Técnica Superior de Ingeniería Aeronáutica y del Espacio (ETSIAE-UPM). The most representative feature of this UAV model is its wing tip configuration composed of 3 semi-wings (grids) which is expected to

improve aerodynamic efficiency by increasing the wingspan during flight. A previous work show that the wing tip configuration with grids generates larger spaced vortices with larger core radii, resulting in lower induced drag than the wing with the same span [15]. To test the effectiveness of these grids, Bennet conducted experimental tests in which the aerodynamic performance increased at low angles of attack, being a good approach for cruise and loiter phase, as well as gliding performances [16]. A preliminary study of computational methods (vortex lattice, method of panels and lift line) was carried out to analyze the aerodynamic performance of the present UAV with the winglets retracted [17]. In this paper, a comparative analysis of numerical and experimental aerodynamic results is presented to investigate the effectiveness of grid technology on wings for several angles of attack. A six-axis force transducer was used to measure the lift and drag in a Low-Speed Wind Tunnel at the Instituto Nacional de Técnica Aeroespacial (INTA). The ANSYS-Fluent software was used to solve the Navier-Stokes Equations and obtain the aerodynamic forces on the vehicle. Both techniques show an increase in aerodynamic efficiency for the cruise and loiter phases with the extended grids.

2.0 BIOMIMETIC UAV MODEL

This section presents the biomimetic UAV model inspired on the primary feathers of an eagle which is a result of a preliminary design developed between the Instituto Nacional de Técnica Aeroespacial and Universidad Politécnica de Madrid 17[]. The design of the UAV is based on a rectangular wing with three grids at the tip of the wing with a gap of 4.5 mm between each of them (see Figure 2-1). The rectangular wing is composed of Eppler 186 airfoils while the grids of NACA 0012 airfoils. The three winglets present zero taper ratio and sweep and with the same angle of attack as the rectangular wing. The chord of the wing is 90 mm along the wingspan while the chord of the grids is 20 mm. The wingspan of the UAV configuration with the grids retracted is 540 mm and when the grids are extended this dimension reaches 720 mm. To control the UAV, a V-tail is selected following the constitution of birds.

In this paper, the two UAV configurations (with retracted and extended grids) are numerical and experimentally studied, as it will be explained in the following sections. The geometrical features of the biomimetic UAV are presented in Table 2-1.

Table 2-1. Geometrical features of the biomimetic UAV.

UAV Configuration	Retracted grids	Extended grids
Aspect Ratio	6	8
Wingspan (*m*)	0.54	0.72
Chord (*m*)	0.09	0.09
Wing area (m^2)	0.0486	0.0648

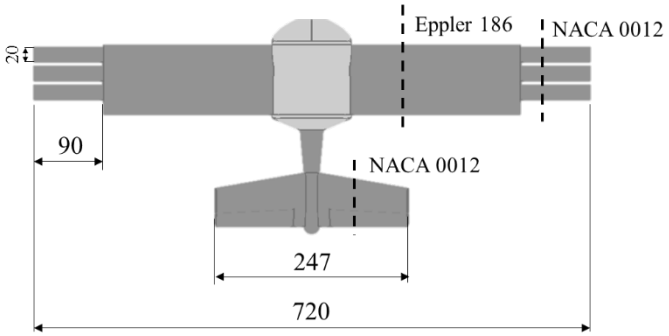

Figure 2-1. Biomimetic UAV with extended grids.

3.0 NUMERICAL SIMULATIONS

The computational analysis has been performed by solving the Navier-Stokes equations using ANSYS-Fluent software. The control volume in Figure 3-1 shows the computational flow domain with the different boundary conditions. The flow enters through the inlet, crosses the control volume where the UAV model is located and exits through the outlet. All faces (Inlet, Outlet, S_2, S_3 and S_4) need to be placed sufficiently far away from the model so they do not have a negative effect on the numerical solution except the S_1 face which is the symmetrical boundary condition and has to be located just in the symmetrical model plane. The inlet boundary is located 6 wing chords upstream of the leading edge of the wing while the outlet boundary is placed at 20 chords downstream of the trailing edge of the wing. Only half of the model is calculated because the freestream velocity is along the chordwise direction (X-axis) and the effect of the propeller has not been considered which results in a shorter processing time to find the convergence solution at the same time less memory, storage and processing capability requirements.

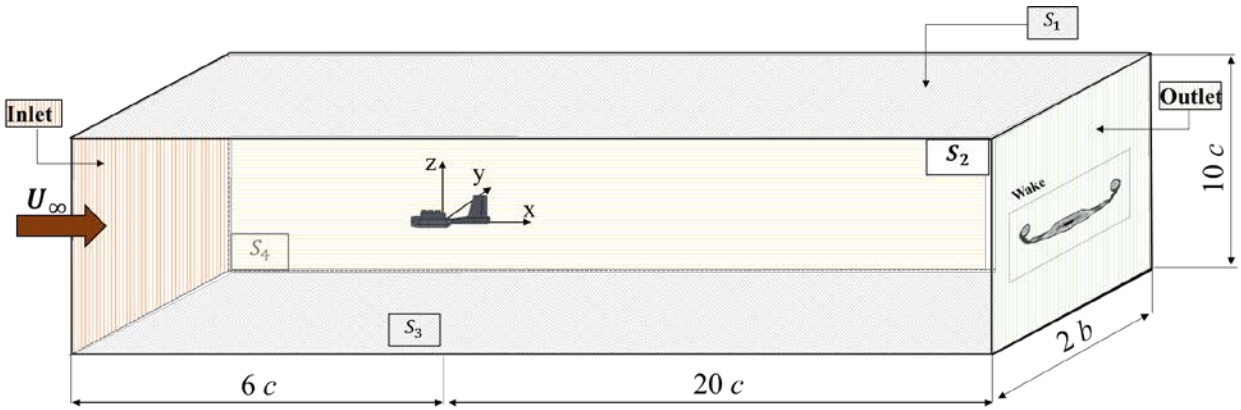

Figure 3-1. Dimensions of the computational flow domain and the boundary conditions.

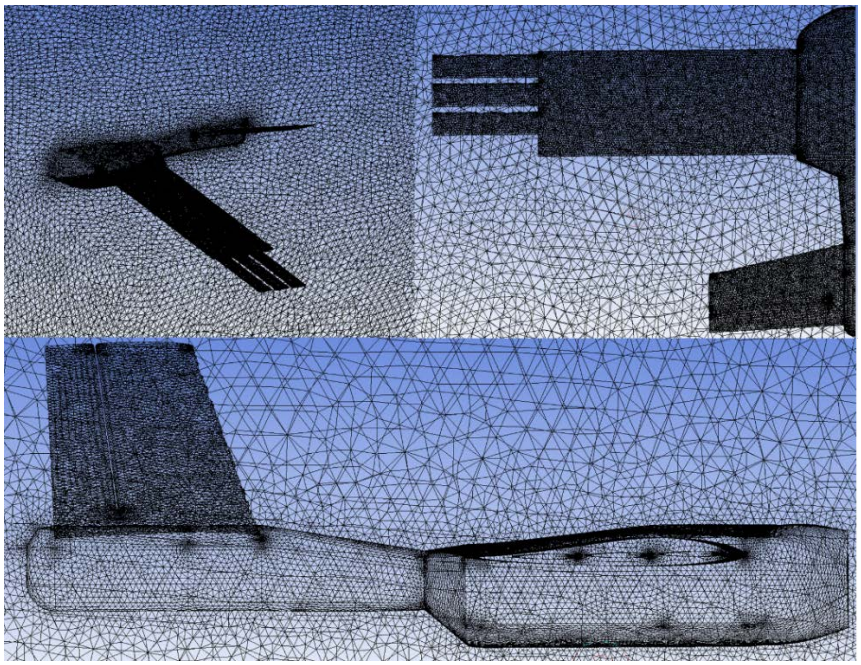

Figure 3-2. Details of the unstructured mesh.

Due to the complex geometry of this UAV model, an unstructured mesh of tetrahedral cells in all flow domain is used. The unstructured mesh in each numerical simulation is generated by approximately 5 millions elements. Figure 3-2 shows several views of the unstructured mesh.

This study is focused on the steady state flow over the rectangular wing for the two UAV configurations (extended and retracted grids) and for several angles of attack. The Reynolds-Average Navier Stokes (RANS) equations are solved by using the pressure-based solver. The flow turbulence is modelled by using the k-omega turbulence model and the incoming flow presents a level of turbulence intensity lower than 1.0 %. All numerical simulations are initialized by using the inlet velocity of 16 m/s and each simulation is run with a total number of iterations of 1000.

4.0 EXPERIMENTAL SET-UP

The experimental tests were carried out in the Low-Speed Wind Tunnel of the Instituto Nacional de Técnica Aeroespacial (INTA) in Madrid (INTA). This wind tunnel presents a closed circuit with an elliptical open test section of 6 m2 (see Figure 4-1). The test section has a moving platform with streamlined leading and trailing edges to reduce the flow interferences. A DC engine of 450 kW (working at 420 V), located at the opposite side of the test section, feeds the wind tunnel to allow a maximum airflow speed of 60 m/s. The turbulence intensity is lower than 0.5 %. Two different UAV configurations were tested: retracted grids and extended grids (see section II). The UAV models tested on the wind tunnel were manufactured by 3D printing machine since this technique presents encouraging advantages (cost-effective, time-saving and high accuracy) for preliminary aerodynamic studies [16,17]. Nevertheless, the sanding process has been necessary on the wing surfaces and on the grids, thus avoiding the presence of undesired additive material on them, which generates surface roughness and, therefore, less accurate results. The additive material used is Acrylonitrile Butadiene Styrene (ABSplus) and both UAV models are manufactured in full scale (1:1) due to their small dimensions.

All experimental tests were conducted at 16 m/s which corresponds to a Reynolds number based on the wing chord (c = 90 mm) of $9.2 \cdot 10^4$. The UAV model is located in the streamlined support strut which includes a fairing structure to minimize the interference with the flow (as it can be seen in Figure 4-1), and also avoid force erroneous measurements. The tests have been performed at several angles of attack from α=-10° to α=25°.

The UAV model attached to the strut is mounted on a six-axis force transducer to measure the aerodynamic forces (see Figure 4). An ATI Mini40 was used to obtain the drag (D) and lift (L) of the UAV model with extended and retracted grids. The force transducer is connected to a signal amplifier, therefore the output values are presented in voltage. To transform the electrical signal into force, a Labview software was developed to store the data acquisition including a post-processing algorithm. The manufacturer provides the calibration matrix. To obtain the average value of the forces, a recording time of 4 minutes with a sampling time of 1993 Hz was selected. It is important to note that the ATI Mini40 transducer was just placed on the center of gravity of the UAV model. In this case, the reference frame of the resulting force is the body axis, therefore the drag and lift are obtained by projecting the recorded values on the wind axis. Moreover, the tare test to remove the weight load was performed at the initial stage with zero wind tunnel velocity.

The aerodynamic forces are presented by non-dimensional parameters using the classical method of aerodynamic coefficients, as follow:

$$C_L = \frac{L}{\frac{1}{2}\rho V^2 S_{ref}} \tag{1}$$

$$C_D = \frac{D}{\frac{1}{2}\rho V^2 S_{ref}} \tag{2}$$

Where C_L and C_D are the lift and drag coefficients, respectively, L and D are the lift and drag forces, respectively, ρ is the flow density (equal to $1.225\ kg/m^3$), U_∞ is the freestream velocity ($16\ m/s$) and S_{ref} is the reference wing area.

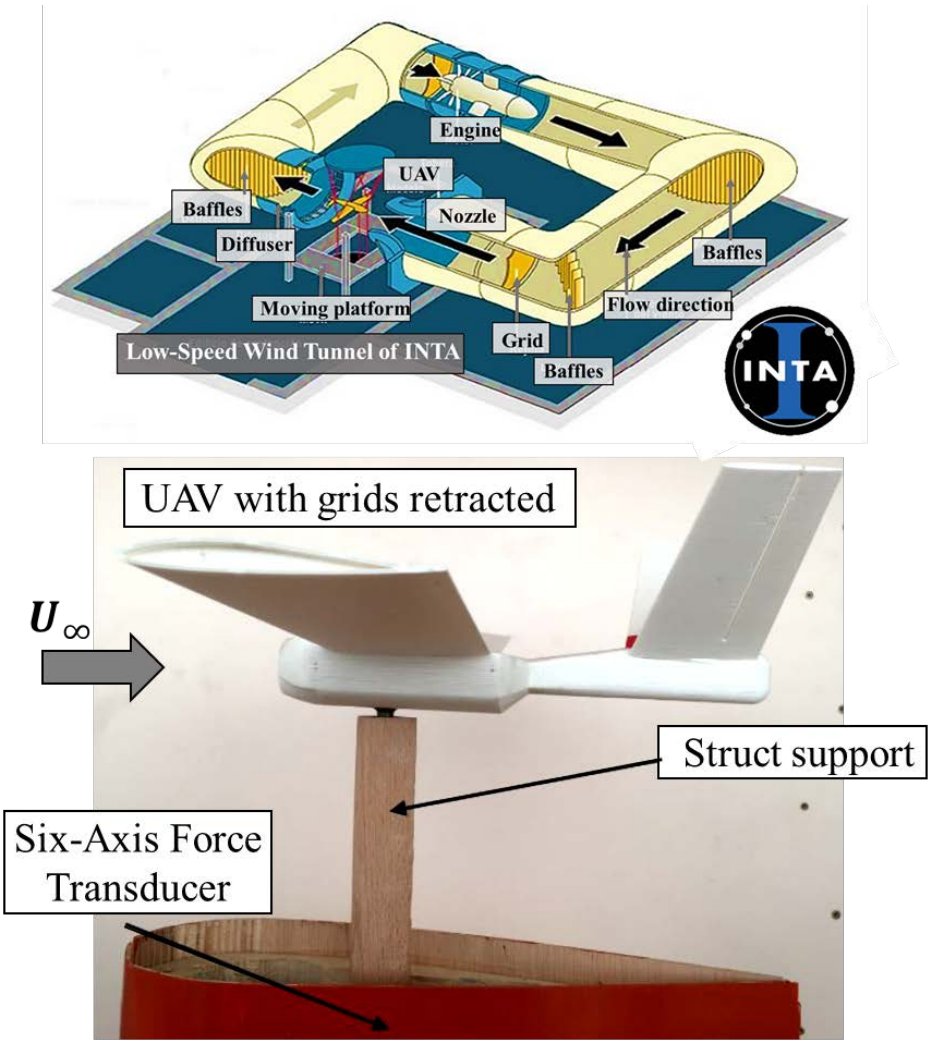

Figure 4-1. Low-Speed Wind Tunnel Components of INTA (above) and experimental set-up (below).

5.0 DISCUSSION OF RESULTS

5.1 Lift coefficient

The lift coefficient versus angle of attack is presented in Figure 5-1 for the two UAV configurations (extended and retracted grids) obtained by numerical simulations and wind tunnel testing. The numerical data is presented by dotted lines and the experimental data by dots. The results clearly show two different regimes, above and below the value of zero degrees of angle of attack. The lift coefficient increases approximately lineal with positive angles of attack until 10°. For positive angles of attack, the lift force generated by the extended grids

configuration (red) is higher than that of retracted grids (blue). However, opposite trend is presented for negative angles of attack.

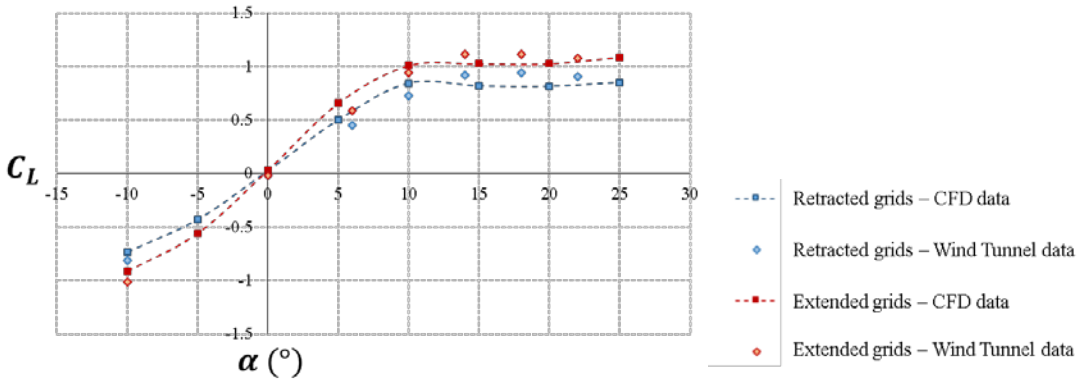

Figure 5-1. Lift coefficient versus angle of attack for the UAV configuration with extended and retracted grids.

5.2 Drag coefficient

Figure 5-2 shows the drag coefficient versus angle of attack obtained by numerical simulations and wind tunnel testing for the two UAV configurations (red for extended grids and blue for retracted grids). The minimum drag coefficient for the two UAV configurations is obtained with zero angle of attack ($C_D = 0.051$ for retracted grids and $C_D = 0.060$). The drag increases with positive and negative values of angle of attack. This increase is not very rapid until $\pm 5°$ in both configurations, however it gradually becomes more pronounced with higher and lower angles of attack. The configuration with extended grids shows a high value of drag during all angles of attack due to its higher wingspan, however in the range of $\pm 5°$, this increase is around 16 % higher than that of retracted grids.

In this graph it can be observed a good agreement between the numerical and experimental data as they present the same trend and the drag coefficient values show a relative error of 5 % or lower for the low values of angles of attack.

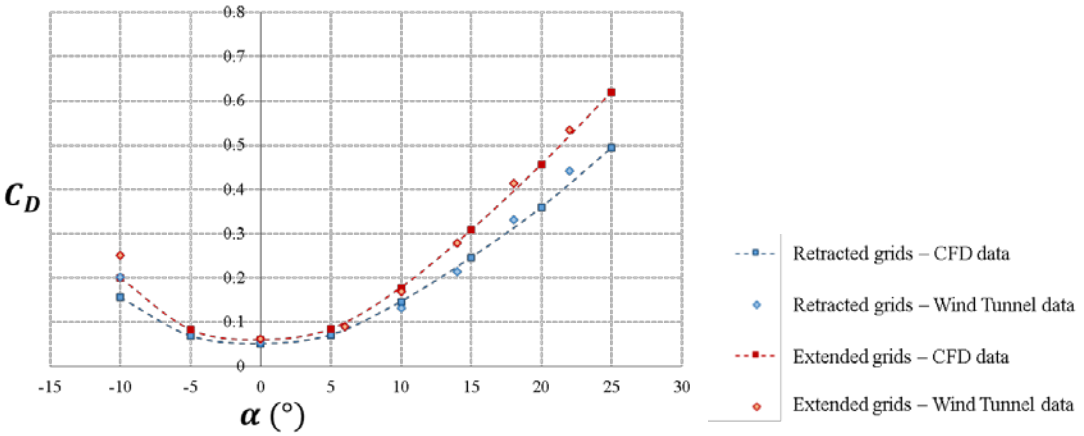

Figure 5-2. Drag coefficient versus angle of attack for the UAV configuration with extended and retracted grids.

5.3 Drag Polar

Figure 5-3 shows the polar curves obtained by numerical simulations and wind tunnel testing and plotted as the drag coefficient versus lift coefficient for the two UAV configurations. As it can be seen in Figure 5-3, the zero lift coefficient for both UAV configurations is obtained for the angle of attack of 0°. Figure 7 shows that for a constant value of the lift coefficient, except for the zero lift value, more drag is generated with the grids retracted.

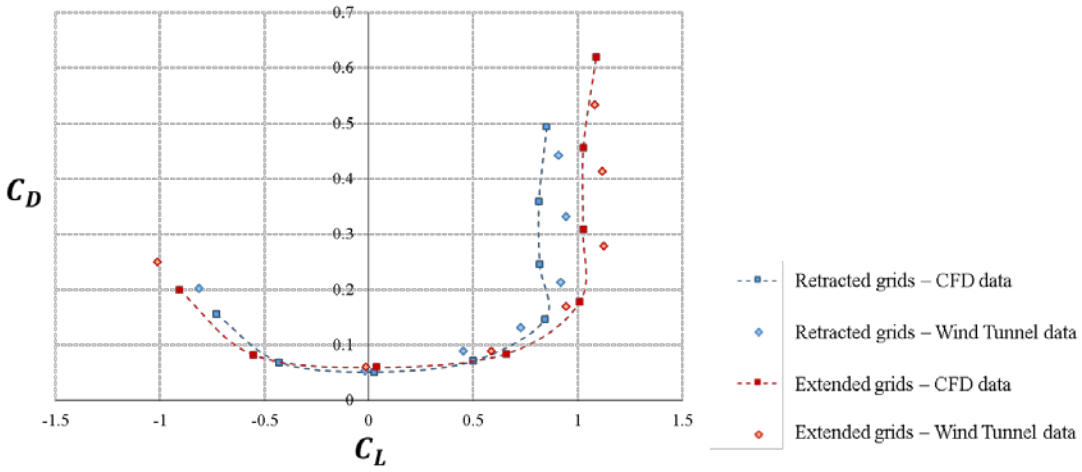

Figure 5-3. Drag polars for the UAV configuration with extended and retracted grids.

5.4 Aerodynamic efficiency

Figure 5-4 shows the relation between lift coefficient C_L and drag coefficient C_D at several angles of attack. It is very clear that the UAV needs to generate as much lift with as little drag as possible. From the Figure 5-1 (C_L vs. α), the maximum lift for both UAV configurations (retracted and extended grids) is obtained for $\alpha > 10^{\circ}$ and from the Figure 5-2 (C_D vs. α), the minimum drag coefficient for both UAV configurations is achieved with zero angle of attack.

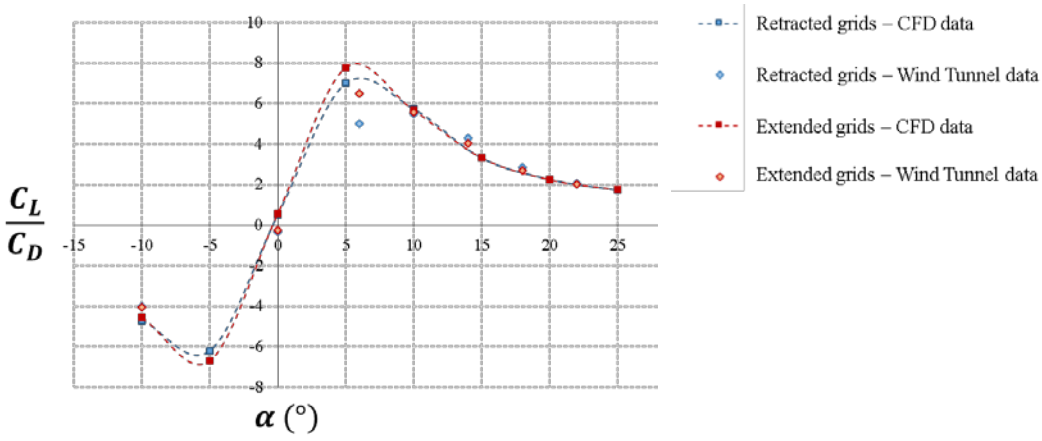

Figure 5-4. Aerodynamic efficiency for the UAV configuration with extended and retracted grids.

Looking at Figure 5-4, none of the previous scenerarios give the best C_L/C_D ratio. In the cruise phase ($\alpha = 0^{\circ}$), the lift coefficient is 0.57 times the drag coefficient for the extended grid configuration and approximately

0.50 times for the retracted grid configuration. The C_L/C_D ratio increases very rapidly up to 5º, at which angle of attack the lift coefficient is around 7.77 times the drag coefficient for extended grid configuration and approximately 7.01 times for the retracted grid configuration. From that angle of attack on the $\frac{C_L}{C_D}$ ratio in both UAV configurations decreases gradually mainly because drag grows more rapidly than lift. At $\alpha = 5^{\circ}$, the C_L/C_D ratio reaches its maximum value for both UAV configurations. At $\alpha > 5^{\circ}$, the relation between C_L and C_D presents approximately the same value for both UAV configurations.

Additionally, to summarize the main aerodynamic variations between the two UAV configurations, Figure 5-5 shows the percentage variation in lift coefficient (ΔC_L (%)), drag coefficient (ΔC_D (%)), and aerodynamic efficiency (ΔE (%)) of the UAV with extended grids compared to the UAV with retracted grids.

The data show that for cruise and loter phases ($\alpha = 0^{\circ}$ and $\alpha = 5^{\circ}$) the extended grid configuration presents a higher aerodynamic efficiency than the retracted grid configuration, so the grid will be extended only for these phases while for the landing and take-off phases they will be retracted.

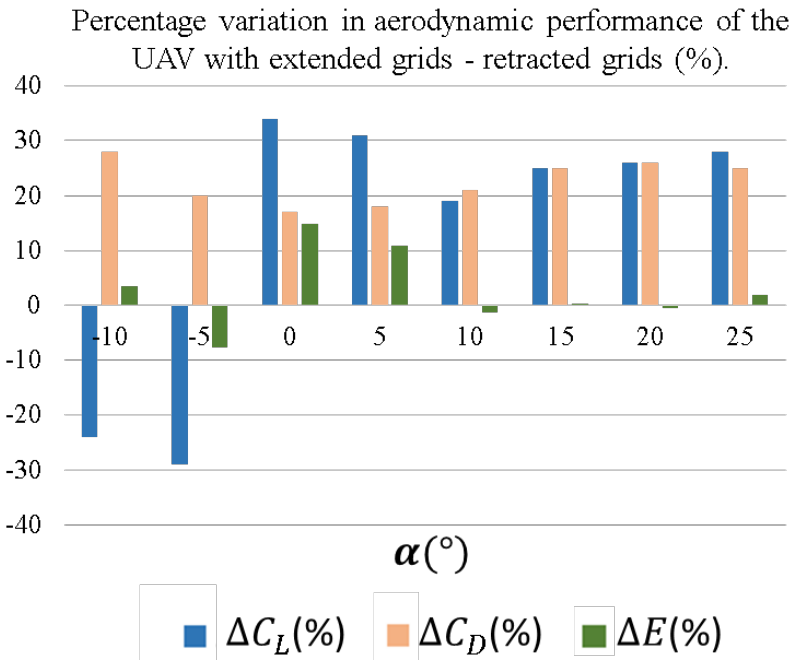

Figure 5-5. Percentage variation in aerodynamic performance of the UAV configuration with extended grids respect to the configuration with retracted grids.

5.5 Flow visualization

Additionally, in this section a global visualization of the flow around the rectangular wing with retracted and extended grids of the most representative angles of attack is presented (see Figure 5-6). Two perpendicular planes at the half of the wing and at the wing tip are visualized along with the streamlines. The orange pattern shows the freestream velocity of 16 m/s. At $\alpha = 5^{\circ}$, the flow is completely attached in both UAV configurations. At $\alpha = 10°$, the flow is still attach on the rectangular wing for both UAV configurations, however there is a flow detachment around the grids (at the tip of the wing) when they are extended which results to stall entry taking place through the wing tip towards the symmetry axis. Finally, at $\alpha = 15^{\circ}$, the recirculation bubble of low velocities is generated over the wing for both UAV configurations which deteriorates the aerodynamic performances.

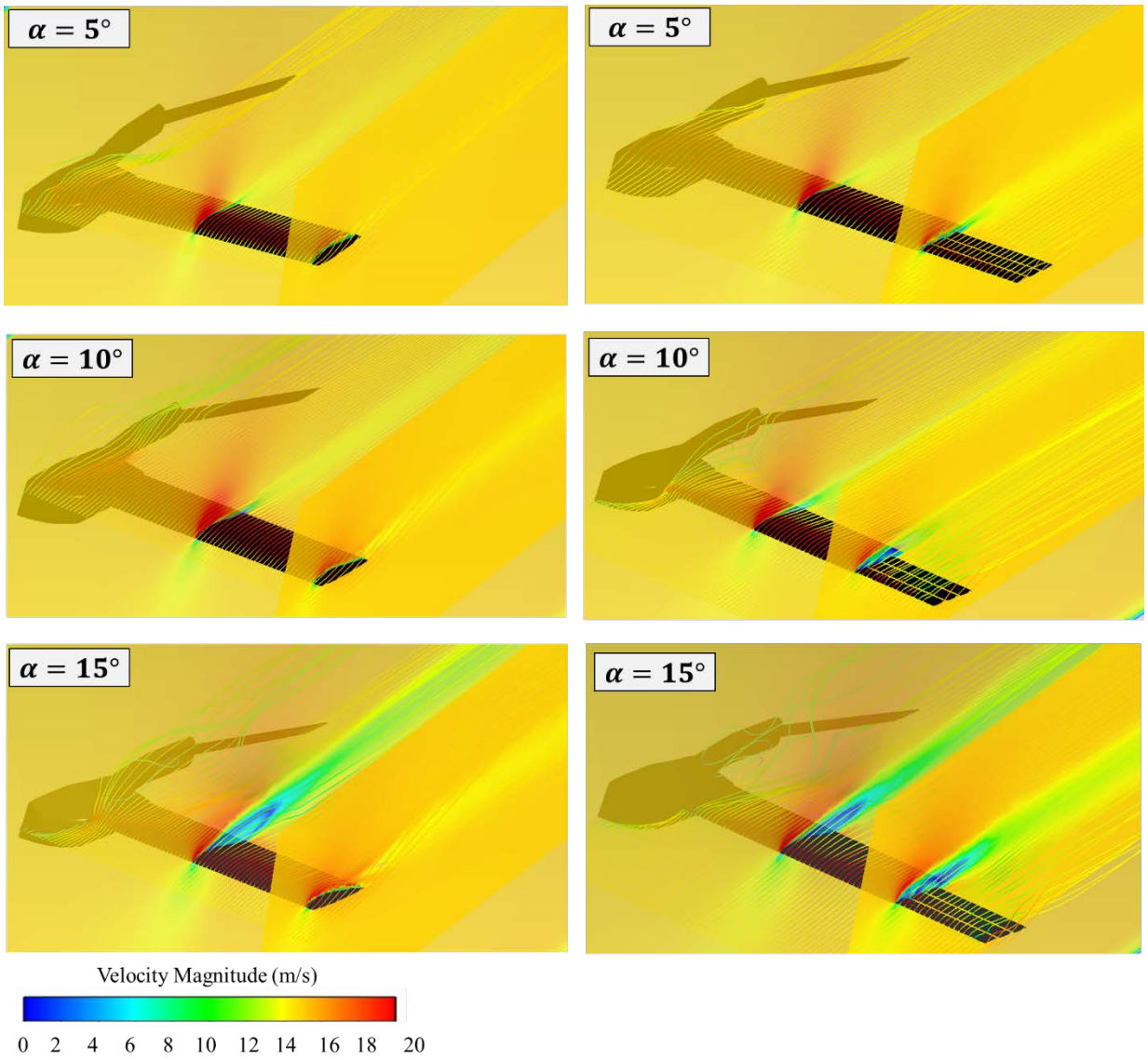

Figure 5-6. Velocity magnitude at ½ b and at the tip of the wing for 5, 10 and 15º for the two UAV configurations: retracted and extended grids.

6.0 CONCLUSIONS

This paper presents a numerical and experimental study of a biomimetic 50 cm UAV inspired on the primary feathers of an eagle. The configuration of the UAV is based on a rectangular wing with three grids at the tip of the wing and V-tail. The flight regime analyzed is $Re = 9.2 \cdot 10^4$, which corresponds to 16 m/s, a normal operating regime of these type of vehicles.

The aerodynamic coefficients have been obtained by using ANSYS-fluent software and a six-axis force transducer in the wind tunnel. The numerical and experimental data have shown a good agreement with a relative error in drag coefficient of 5 % or lower for low angles of attack ($-5^{\circ} \leq \alpha \leq 5^{\circ}$).

Finally, the results have shown that for cruise and loiter conditions the grids should be extended since the aerodynamic efficiency is higher, while for landing and take-off maneuvers they should be retracted.

References

[1] Jiakun Han, Zhe Hui, Fangbao Tian, and Gang Chen,''Review on bio-inspired flight systems and bioinic aerodynamics'', Chinese Journal of Aeronautics, 34(7): 170-186, 2021.

[2] A.C. Carruthers, S.M.Walker, A.L.R. Thomas and G.K.Taylor, ''Aerodynamics of aerofoil sections measured on a free-flying bird'', Proc. IMechE Vol. 224 Part G:J. Aerospace Engineering, doi: 10.1243/09544100JAERO737, 2009

[3] Marco KleinHeerenbrink and Anders Hedenström, ''Wake analysis of drag components in gliding flight of a jackdaw (Corvus monedula) during moult'', Interface Focus 7: 20160081, http://dx.doi.org/10.1098/rsfs.2016.0081, 2016.

[4] Vance A. Tucker, ''Gliding Birds: Reduction of Induced Drag by Wing Tip Slots between the Primary Feathers'', J. exp. Biol. 180, 285-310 (1993).

[5] Marco KleinHeerenbrink, L. Christoffer Johansson and Anders Hedenström, ''Multi-cored vortices support function of slotted wing tips of birds in gliding and flapping flight'', J. R. Soc. Interface 14: 20170099, http://dx.doi.org/10.1098/rsif.2017.0099.

[6] Mostafa Hassanalian, Abdessattar Abdelkefi, Mingjun Wei and Saeed Ziaei-Rad, ''A novel methodology for Wing Sizing of bio-inspired flapping wing Micro Air Vehicles: Theory and Prototype''Acta Mech 228, 1097-1113 (2017), doi: 10.1007/s00707-016-1757-4.

[7] H.J. Shim and S.O.Park, ''Low-speed wind-tunnel tests results of a BWB-UCAV model'', Procedia Engineering 67, 50-58, doi: 10.1016/j.proeng.2013.12.004, 2013.

[8] Mochammad Ariyanto, Joga D. Setiawan, Teguh Prabowo, Ismoyo Haryanto, Munadi ''Design of a Low-Cost Fixed Wing UAV'', IJCAET & ISAMPE 2017.

[9] Marek, P. L., "Design, optimization and flight testing of a micro air vehicle" Doctoral dissertation, University of Glasgow, 2008.

[10] Austin, R. (2011). Unmanned aircraft systems: UAVS design, development and deployment (Vol. 54). John Wiley & Sons.

[11] Moschetta, J. L. "The aerodynamics of micro air cehicle: technical challeges and scientific issues," International Journal of Engineering Systems Modelling and Simulation, Vol. 6, No. 3/4, 2014, pp. 134-148. ISSN 1755-9758.

[12] Smith, M., Komerath, N., Ames, R., Wong, O., & Pearson, J. (2001). Performance analysis of a wing with multiple winglets. In 19th AIAA Applied Aerodynamics Conference (p. 2407).

[13] Flake, J., Frischknecht, B., Hansen, S., Knoebel, N., Ostler, J., &Tuley, B., "Development of the Stableyes Unmanned Air Vehicle", 8th International Micro Air Vehicle Competition, The University of Arizona, Tucson, AZ, 2004, pp. 1-10.

[14] Zheng Min , Vu Khac Kien & Liew J.Y. Richard (2010) Aircraft morphing wing concepts with radical geometry change, The IES Journal Part A: Civil & Structural Engineering, 3:3, 188-195, DOI: 10.1080/19373261003607972

[15] La Roche, U., & Palffy, S. (1996, September). Wing-grid, a novel device for reduction of induced drag on wings. In ICAS PROCEEDINGS (Vol. 20, pp. 2303-2309).

[16] Bennett, D. (2001). The Wing Grid: A New Approach to Reducing Induced Drag.

[17] Barcala-Montejano, M. A., Rodríguez-Sevillano, A. A., Bardera-Mora, R., García-Piqueras, M. D. Fabricación mediante prototipado rápido de un micro UAV (MAV) biomimético controlado por wing grids. Congreso CivilDRON'16. 26-27 enero 2016. Libro de actas. (spanish).